Ab initio and shell model studies of structural, thermoelastic and vibrational properties of SnO_2 under pressure

2013 J. Phys.: Condens. Matter 25 135404

(http://iopscience.iop.org/0953-8984/25/13/135404)

IOP PUBLISHING JOURNAL OF PHYSICS: CONDENSED MATTER

J. Phys.: Condens. Matter **25** (2013) 135404 (11pp) doi:10.1088/0953-8984/25/13/135404

Ab initio and shell model studies of structural, thermoelastic and vibrational properties of SnO_2 under pressure

R A Casali[1], J Lasave[2], M A Caravaca[3], S Koval[2], C A Ponce[1] and R L Migoni[2]

[1] Departamento de Física, Facultad de Ciencias Exactas y Naturales y Agrimensura UNNE, Avenida Libertad 5600, 3400 Corrientes, Argentina
[2] Instituto de Física Rosario, CONICET and Universidad Nacional de Rosario, 27 de Febrero 210 Bis, 2000 Rosario, Argentina
[3] Departamento de Físico-Química, Facultad de Ingeniería, UNNE, Avenida Las Heras 727, 3500 Resistencia, Argentina

E-mail: lasave@ifir-conicet.gov.ar

Received 29 December 2012, in final form 6 February 2013
Published 7 March 2013
Online at stacks.iop.org/JPhysCM/25/135404

Abstract

The pressure dependences of the structural, thermoelastic and vibrational properties of SnO_2 in its rutile phase are studied, as well as the pressure-induced transition to a $CaCl_2$-type phase. These studies have been performed by means of *ab initio* (AI) density functional theory calculations using the localized basis code SIESTA. The results are employed to develop a shell model (SM) for application in future studies of nanostructured SnO_2. A good agreement of the SM results for the pressure dependences of the above properties with the ones obtained from present and previous AI calculations as well as from experiments is achieved. The transition is characterized by a rotation of the Sn-centered oxygen octahedra around the tetragonal axis through the Sn. This rotation breaks the tetragonal symmetry of the lattice and an orthorhombic distortion appears above the critical pressure P_c. A zone-center phonon of B_{1g} symmetry in the rutile phase involves such rotation and softens on approaching P_c. It becomes an A_g mode which stabilizes with increasing pressure in the $CaCl_2$ phase. This behavior, together with the softening of the shear modulus $(C_{11} - C_{12})/2$ related to the orthorhombic distortion, allows a precise determination of a value for P_c. An additional determination is provided by the splitting of the basal plane lattice parameters. Both the AI and the experimentally observed softening of the B_{1g} mode are incomplete, indicating a small discontinuity at the transition. However, all results show continuous changes in volume and lattice parameters, indicating a second-order transition. All these results indicate that there should be sufficient confidence for the future employment of the shell model.

(Some figures may appear in colour only in the online journal)

1. Introduction

Tin dioxide (SnO_2 or stannic oxide) is a material with important technological applications in solar cells, gas sensors, optoelectronic devices, and lithium-ion batteries [1]. It was one of the first oxides considered, and is still the most frequently used, for gas sensing applications exhibiting high sensitivity by variation of the electrical conduction. The gas sensitivity of these oxides is in a close relationship with their surface chemical activity, i.e. a larger surface-to-volume ratio implies a more sensitive sensor. Actually, electronic properties of SnO_2 nanodevices are strongly influenced by surface processes, with a sensitivity superior to those of their thin film counterparts [2]. Thus, it would be desirable to model the structure and the physical behavior of the nanostructured material. With the purpose of performing such modeling in

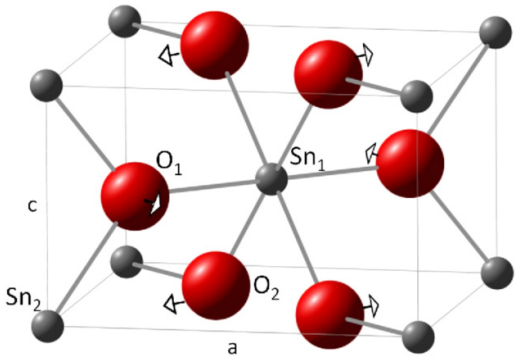

Figure 1. Schematic representation of the rutile structure of SnO_2. The arrows indicate the rotation of the oxygen octahedron corresponding to the B_{1g} soft mode.

future work, we focus now on the development of an atomistic model for SnO_2.

Stannic oxide belongs to the rutile-type group and undergoes the following sequence of structural phase transitions under increasing high pressure: rutile-type phase → $CaCl_2$-type phase → α-PbO_2-type phase → fluorite-type cubic phase [3]. The low-pressure phase of SnO_2 is a rutile-type structure with two formula units in a simple tetragonal cell. Each Sn atom is at the center of a regular oxygen octahedron (see figure 1). The transition to the $CaCl_2$-type structure with pressure corresponds to a small rotation of these octahedra around the tetragonal axis and the deformation to an orthorhombic cell occurring in a continuous way, which indicates a second-order transition [3]. This transition has been studied by several experimental [4–6] and theoretical methods [7–9]. It has been also found and extensively analyzed for other isomorphous compounds [10–15]. Raman spectroscopy under pressure has revealed for SnO_2 a critical pressure $P_c \approx 14.8$ GPa [6], which is somewhat higher than the previous value determined using x-ray diffraction, of 11.8 GPa [3]. Brillouin and Raman scattering spectroscopy determined that this transition may be described as pseudoproper ferroelastic. It can be explained by a bilinear coupling of the order parameter associated with a B_{1g} soft phonon, which involves precisely the aforementioned octahedra rotations, and an acoustic mode with the same symmetry [6]. Theoretical *ab initio* calculations at the B3LYP level [7] have predicted $P_c \approx 12$ GPa. A study using the linearized augmented plane-wave method (LAPW) [8] leads to $P_c = 12.4$ GPa (GGA) and 10.1 GPa (LDA).

Detailed investigations of the lattice dynamics in the low-pressure rutile phase of SnO_2 have been carried out in the past. Katiyar and co-workers have measured the polarized infrared reflection, absorption and Raman spectra, and from these data dielectric parameters and the optically active phonon frequencies were determined [16]. In the same work, the dispersion curves for phonons in various symmetry directions were obtained with a rigid-ion model, in good agreement with the experimentally observed frequencies. Using a previously derived shell model for TiO_2, Gervais and Kress slightly readjusted some parameters for SnO_2 and calculated the optical frequencies at the Brillouin-zone center, in rather good agreement with the available experimental data [17]. The temperature dependence of the A_{1g} mode linewidth in the first-order Raman spectrum of SnO_2 was also analyzed in terms of a shell model [18]. Later, the phonon dispersion relations for rutile SnO_2 were determined from *ab initio* calculations as a function of pressure [9]. The latter calculations showed the soft behavior under pressure of the B_{1g} mode. This couples with a transverse acoustic (TA) phonon branch along the Γ–M direction of the Brillouin zone, associated with the elastic shear modulus $C_s = (1/2)(C_{11} - C_{12})$, which also softens with increasing pressure and leads to a ferroelastic phase transition [6]. The elastic constants have been determined from experiments at normal pressure [19] and their pressure dependences were also derived from experimental data [6], and calculated theoretically from first principles [20].

It is worth mentioning here that the structural and vibrational properties of an SnO_2 nanoparticle depend on stresses induced by the morphology and surface termination. Therefore a reliable modeling requires the detailed reproduction of the structural and dynamical behavior under pressure. On account of the restructurations occurring at the nanoscale, it is particularly important that the model describes the structural transition driven by pressure.

Although *ab initio* (AI) calculations are a powerful tool for accurate studies of static, elastic and vibrational properties in the bulk of crystals, the application of these techniques to systems with a large number of atoms (nanoparticles, surfaces, crystals with defects, crystals exhibiting phase transitions, etc) are usually precluded. Moreover, first-principles studies of the dynamic behaviors of systems comprising large number of atoms are almost prohibited, since the CPU time required to perform these simulations is exceedingly large. To overcome this limitation, atomistic models fitted to first-principles and experimental data were usually developed with the requirement of accurately describing the physical properties of the bulk crystals. Such models make the above mentioned large-scale and/or long-time simulations feasible [21–25]. Therefore, in the present work we have determined interatomic potentials for the well-known shell model (SM) applied to the case of SnO_2. Unlike the situation for previous works [17, 18], interatomic potentials are needed in the present case to describe structural transitions and large distortions under pressure.

We report here the results of a study of structural, thermoelastic and vibrational properties under pressure as well as ferroelastic instabilities in SnO_2 based in AI and SM methods. To the best of our knowledge, this is the first study of a ferroelastic transition induced by pressure in SnO_2 performed with the combined use of first-principles and shell model calculations. It can be considered as a test of the capabilities of each method for reproducing the ferroelastic structural instability and other properties under pressure. The SM developed will serve in a future work as a model for studying SnO_2 nanoparticles with different morphologies.

The paper is organized as follows. In the next section we describe the computational methods (*ab initio* and atomistic simulations). Section 3 is devoted to the description of the results for the rutile structure, the rutile–$CaCl_2$-type transition

and elastic properties with pressure. We also describe in this section the phonons in the rutile phase and the lowest Raman mode in both structures. We analyze their dependences with pressure, and also determine the phonon dispersions and the density of states in the low-pressure phase. Finally, we discuss and elaborate on the conclusions in section 4.

2. Computational methods

2.1. Ab initio calculations

The SIESTA code [26] is used in this paper for calculating total energies, atomic forces and stresses. This is achieved by solving the electronic quantum-mechanical equations by means of the density functional approach in the local density approximation (LDA) parameterized by Ceperley and Alder. The interactions between electrons and core ions are simulated through separable Troullier–Martins norm-conserving pseudopotentials [27]. The basis set is constructed with pseudoatomic orbitals (PAOs) of Sankey–Niklewski type, generalized to include multiple-zeta decays which are used to represent the valence wavefunctions. We have generated the atomic pseudopotentials for the atoms of the compound. After extensive tests with $4d^{10}$ electrons in the core or in the valence set of the Sn atom, we found that the inclusion of the 4d shell in the core provides better equilibrium volumes, electronic structures and phonon frequencies compared with experiments. We recall that reliable pseudopotentials are required for phonon calculations. With our selection of pseudopotential, basis set (DZ), orbital confinement (100 meV) and cutoff energy grid (350 Ryd) we found a root mean square error of ≈2% in the comparison with eight measured phonon frequencies [5, 17]. Thus, we have generated the atomic Sn pseudopotentials using the [Kr $4d^{10}$] $5s^2$ $5p^2$ atomic configuration. The cutoff radii selected for *ab initio* generated atomic pseudopotentials were 2.37, 2.43 and 2.75 au for the $5s^2$, $5p^2$ and $5d^0$ angular momentum pseudopotentials respectively. For oxygen we have used 1.15 au for the s and p channels and 0.8 au for the d and f channels. All pseudopotentials are transformed according to the methodology prescribed by Kleinman and Bylander [28]. The elastic constants were determined at the equilibrium rutile phase structure which was obtained by minimizing the total energy with respect to the atomic coordinates and cell parameters. The Kohn–Sham eigenstates were expanded in a numerical orbitals basis set. Our calculations are based on extensive tests of the following basis sets: double-zeta (DZ), double-zeta polarized (DZP), single-zeta (SZ) and single-zeta polarized (SZP), including different degrees of atomic orbital confinement. The best compromise between accuracy in the Raman frequencies and efficiency was found with the use of the DZ basis set. The real space cutoff energy E_c corresponding to 350 Ryd was used to expand the electronic wavefunctions, and the reciprocal space includes 567 k-points in a $20 \times 20 \times 20$ uniform grid for the six-atom primitive cell of rutile with two formula units. The total energy and stress differences were converged to better than 0.1 meV and 0.02 GPa per formula unit.

A conjugate gradient scheme was used to relax the ions, and steepest descents were employed to optimize cell parameters. The details of the method have been given elsewhere [29]. Elastic constants were determined by the method described in [30–32], where a set of small strains e_{ij} are applied to the cell to obtain the elastic constants C_{ijkl}. Due to the symmetry of the rutile structure, six elastic constants are independent [31, 33], which are calculated as functions of pressure. The zone-center phonons were determined by diagonalization of the dynamical matrix D within the frozen phonon approximation using the Vibrator utility of the SIESTA code. The results are compared to findings from Raman and IR experiments [6, 34]. Only the primitive cell is needed for the calculation of the zone-center phonons. Using symmetry information of the tetragonal rutile phase of SnO_2, 36 displacements (six atoms with six displacements each) were needed to construct the required force constants matrix and from it the dynamical matrix. Diagonalization of the calculated dynamical matrix yielded the frequencies and eigenvectors of 18 zone-center phonons.

2.2. The shell model

The electronic polarizabilities of the ions are represented in the shell model by an electronic shell of charge Y coupled harmonically with a constant K to the core. In the present model the electronic polarizability of the Sn^{+2} ion is neglected, while an isotropic polarizability is assigned to the O^{-2} ion. For the interactions between different ions this model takes into account the short-range shell–shell repulsive interactions arising from the wavefunction overlap between neighboring ions up to a certain cutoff as well as the long-range Coulomb interactions between all charged shells and cores [21–25]. In contrast to the Sn atoms, the O atoms are located at sites without inversion symmetry, and hence the equilibrium values of their core and shell positions are different. The short-range repulsive pair potentials for the Sn–O and O–O interactions are taken to be of the Buckingham type, $A\exp(-\frac{r}{\rho}) - \frac{C}{r^6}$, with a cutoff of 9 Å for all pairs. We distinguish two types of oxygen in the oxygen octahedron surrounding each Sn_1 site: four O_2s lying in a vertical plane through the central Sn_1 atom; and two O_1s located on an xy-axis through Sn_1 perpendicular to that plane, on both sides of the Sn_1 (see figure 1). Due to the anisotropic environment of the Sn_1–O_1 and Sn_1–O_2 bonds in the structure, we consider different short-range Sn–O Buckingham potentials for these pairs of atoms. We additionally include a three-body angular potential of the form $\frac{1}{2}k(\theta - \theta_0)^2$ for the O_1–Sn–O_2 bonds inside the octahedron, on account of their partially covalent character. Thus, the model contains 14 adjustable parameters, including the total charges Z of the ions and considering the charge neutrality condition. The calculations of the different quantities corresponding to this model were performed with the GULP code [35].

3. Results

We first determined the model parameters by adjusting them to reproduce the experimental internal structures and lattice

Table 1. Shell model parameters as defined in the text. The first four columns correspond to the parameters of the Buckingham-type potential between a pair of atoms. The next four columns display charges and spring constants of the ions. Z denotes the total charge of each ion. The last three columns show the parameters of the three-body angular potential.

Bond	A (eV)	ρ (Å)	C (eV Å^6)	Ion	Z (e)	Y (e)	K (eV Å^{-2})	Ang. bond	k (eV rad^{-2})	θ_0 (°)
Sn_1–O_1	4166	0.260	10.00	Sn	2.88	0	∞	O_1–Sn–O_2	2.00	90.00
Sn_1–O_2	1350	0.305	0.00	O	−1.44	−1.37	143.51			
O–O	3200	0.285	169.00							

Table 2. AI and SM results for the zero-pressure structural parameters of the rutile phase: lattice constants a and c, the equilibrium volume V, axial compressibilities k_a and k_c, the bulk modulus B and its derivative B'. a and c are in units of Å, and B in GPa. k_a and k_c are in units of 10^{-4} kbar^{-1}, and the cell volume V in Å^3. Experimental data and other theoretical calculations are added for comparison.

	AI	SM	FP-LMTO[a]	Calc.[b]	Calc.[c]	Calc.[d]	Exp.[e]	Exp.[f]
a	4.725	4.580	4.761	4.699	4.715	4.58	4.737	4.738
c	3.263	3.195	3.184	3.165	3.194	3.08	3.186	3.186
u	0.308	0.312	0.306	0.306	0.306	0.304	0.307	—
c/a	0.691	0.698	0.669	0.673	0.677	0.672	0.673	0.673
k_a	1.89	1.51	—	1.389	—	—	1.86	—
k_c	0.74	1.07	—	0.673	—	—	0.99	—
V	72.84	67.03	72.17	69.88	71.01	64.61	71.49	71.42
B	214	200	181	242.4	221	212	205	212
B'	4.5	—	—	4.76	6	—	7.42	5.13

[a] Reference [37].
[b] Reference [20].
[c] Reference [7].
[d] Reference [8].
[e] Reference [3].
[f] Reference [19].

constants [3] of the tetragonal rutile-type phase at $P = 0$ and the orthorhombic $CaCl_2$-type phase at $P = 12.6$ GPa. To this end, we have used the fitting functionality available in the GULP code [35], which enables the structure optimization of the systems at zero temperature and different external pressures. Once the set of parameters was satisfactory for reproducing the structure of both phases, we further refined the model to better adjust some phonons to the *ab initio* data, and to improve its pressure behavior up to 20 GPa, particularly that related to the tetragonal–orthorhombic transition. The final set of SM parameters is presented in table 1.

3.1. The rutile phase and its pressure behavior

Structure. The rutile-type structure of the tin dioxide mineral cassiterite at ambient pressure has the tetragonal space group $P42/mnm$ (see figure 1). The structure is completely determined by three structural parameters: the two lattice constants a and c, and the internal parameter u which defines the oxygen position $(u, u, 0)$. The model structural parameters obtained for ambient pressure are compared with our *ab initio* results calculated with SIESTA in table 2. Also comparison is made with other *ab initio* results and experimental data. The overall agreement is satisfactory; only the lattice parameter a and the volume are somewhat underestimated by the model. The volume dependence of the total energy is obtained *ab initio* with SIESTA. These calculations are performed by fixing different values of the target pressure and relaxing the structure until the stress differences converge to below the tolerance. These results are interpolated using the third-order Birch–Murnaghan E(V) equation to obtain the bulk modulus B and its pressure derivative B'. The result for B is compared with the model value obtained with GULP in table 2. Other *ab initio* and experimental values of this magnitude are also shown in this table. Both AI and SM values obtained with our calculations are in better agreement with experiments than previous *ab initio* results. The theoretical AI value of the pressure derivative B' is in good enough agreement with respect to the experimental value.

Elastic properties. The six elastic constants of the rutile-structured stania were derived from the *ab initio* computed stresses generated by the strain [30]. The behaviors with pressure of the uniaxial, biaxial and shear elastic stiffnesses are shown in figures 2(a)–(c), respectively. Experimental results are available for C_{11}, C_{12}, C_{44} and C_{66} up to approximately 12 GPa [6, 16]. All pressure behaviors show an excellent agreement among the AI, SM and experimental results, with the only exceptions being for C_{13}, C_{33} and C_{44}. Here there are some differences between AI and SM data, but nevertheless very good agreement in the tendencies is shown. The calculated values of C_{44} are the smallest as compared to the other elastic constants and are nearly pressure independent in the whole range studied (see figure 2(c)). This is in accordance with the experimental data of Hellwig *et al* [6] and previous calculations [20, 36].

The results for the zero-pressure elastic constants and their pressure derivatives are compared to results from

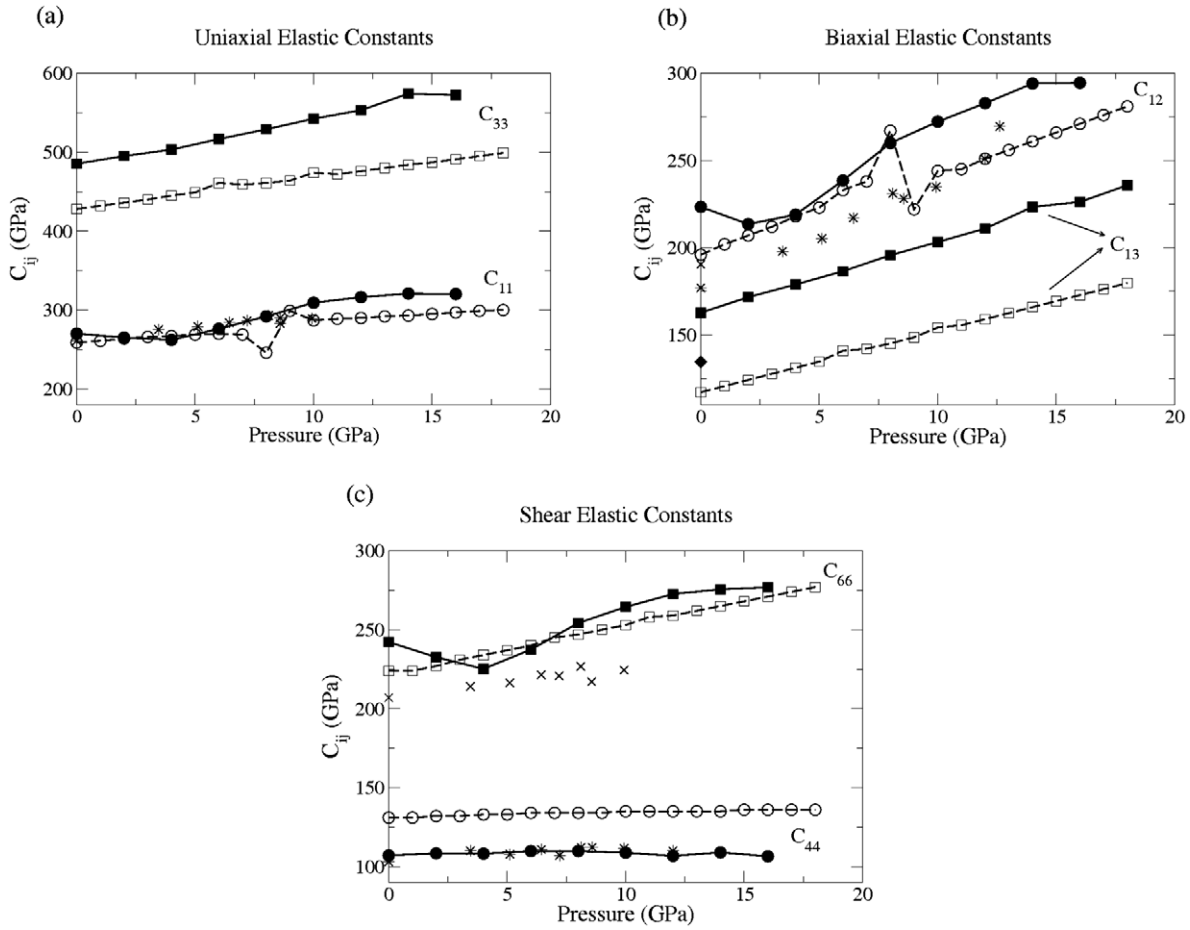

Figure 2. Pressure dependences of (a) uniaxial, (b) biaxial and (c) shear elastic constants for the rutile structure of SnO_2. The solid line and circles represent the AI values while dashed lines and empty circles show the SM results for (a) C_{11}, (b) C_{12} and (c) C_{44}. The AI results for (a) C_{33}, (b) C_{13}, and (c) C_{66} are shown by solid lines and squares while the SM results for these magnitudes are represented by dashed lines and empty squares. The experimental values [6] of (a) C_{11}, (b) C_{12} and (c) C_{44} are denoted by star symbols, and those of (c) C_{66} by cross symbols. Also shown are calculations from [16] of (b) C_{12} (cross symbols) and (b) C_{13} (solid diamonds) at zero pressure.

Table 3. AI and SM results for the zero-pressure elastic stiffness C_{ij} and its pressure derivative C'_{ij} at $P = 0$ GPa in the rutile phase. The results were taken from a fit to a second-degree polynomial $C_{ij}(P) = a + bP + cP^2$ where $a = C_{ij}$ and $b = \frac{dC_{ij}}{dP}|_{P=0} \equiv C'_{ij}$. We also show in the last column results for the derivative of the elastic shear modulus $C'_s \equiv (C'_{11} - C'_{12})/2$. Available experimental data and theoretical calculations are added for comparison. The unit of C_{ij} is GPa, while C'_{ij} is dimensionless.

	C_{11}	C_{12}	C_{13}	C_{33}	C_{44}	C_{66}	C'_{11}	C'_{12}	C'_{13}	C'_{33}	C'_{44}	C'_{66}	C'_s
AI	261	211	161	483	107	232	3.32	5.05	4.07	5.62	0.53	1.11	−0.86
SM	260	197	117	429	131	225	2.23	5.45	3.46	4.68	0.50	3.20	−1.61
Calc.[a]	261	180	150	472	109	223	7.39	7.17	5.05	7.18	1.04	4.27	0.11
Calc.[b]	217	191	134	313	55	194							
Exp.[c]	261	186	—	—	103	207	2.94	4.2	—	—	0.60	1.82	−0.63
Exp.[d]	262	177	156	449	103	207	4.66	6.14	4.51	6.28	0.88	3.15	−0.74

[a] Reference [20].
[b] Reference [16].
[c] Reference [6] up to 14.6 GPa.
[d] Reference [19] up to 1 GPa.

experiments and other calculations in table 3. All magnitudes show a general good agreement in the comparison of the AI and SM results with experimental data. In particular, C_{11} is in excellent agreement with experimental and other calculated values, as is seen also in its pressure behavior (see figure 2(a)). As an exception, the rigid-ion model calculated C_{11} is underestimated [16]. Actually, we see a general underestimation of the elastic constants calculated in [16]. A good accordance is observed as well in table 3 between the elastic constant derivatives calculated here and

Table 4. Polycrystalline thermoelastic properties: bulk (B_0), Young (E_0), and shear (G_0) moduli; Poisson constants (ν); transverse (v_t), longitudinal (v_l) and averaged (v_m) sound velocities; and Debye temperatures (θ_D). All magnitudes were calculated from the elastic constants C_{ij} at $P = 0$ GPa obtained by the AI and SM methods, and using the Reuss–Voigt–Hill approach as explained in the text (for details see [30]).

	AI	SM	Calc.[a]	Exp.[b]	Exp.[c]	Exp.[d]
B_0 (GPa)	225	200	212	203	212	225
G_0 (GPa)	96	108	106	98	101	105
ν	0.31	0.27	0.28	0.29	0.29	0.30
E_0 (GPa)	253	276	273	—	262	273
v_t (m s^{-1})	3707	3811	3898	3750	3809	3879
v_l (m s^{-1})	7167	6794	7119	6910	7046	7232
v_m (m s^{-1})	4150	4241	4346	4184	4252	4332
θ_D (K)	542	549	567	—	555	566

[a] Reference [36].
[b] Reference [42] ($P = 1$ kbar).
[c] Reference [19] ($P = 0$ GPa).
[d] Reference [6] ($P = 3$ GPa).

the experimental ones, as is apparent also in their pressure dependences shown in figure 2. Other *ab initio* calculations give rather overestimated values of these derivatives (see table 3) [20]. The AI result for the derivative of the elastic shear modulus C'_s is in good agreement with the experimental data, although the SM value is overestimated (see the last column of table 3). Unlike previous calculations [20], both AI and SM values are negative, which is consistent with the soft behavior of the transverse acoustic mode associated with the elastic shear modulus on approaching P_c.

We have also calculated polycrystalline mean values of elastic properties on the basis of the knowledge of the different elastic constants. To this end, we followed the procedure explained in [30] and used the Reuss approximations to obtain the arithmetic means of these extremes (the Reuss–Voigt–Hill approach) [31, 33, 38–40]. We show in table 4 the mean values of different elastic moduli, Poisson constants, sound velocities and Debye temperatures calculated with this procedure. These magnitudes are compared to available experimental and theoretical data, showing very good overall agreement. The large values (approaching the upper limit 0.5) found for the Poisson coefficients indicate the ductile character of the material. This is consistent with the results obtained for the B_0/G_0 ratio, 2.34 (AI) and 1.85 (SM), which are larger than the critical value 1.75. The latter signals the ductile/brittle (larger/smaller) behavior of the material [41]. This fact is also verified experimentally, with values in the range 2.07–2.14 (see table 4). Our AI result for the Poisson constant ν is slightly above the SM one, while the experimental data lie in between. The smaller SM value of ν may be ascribed to a slight overestimation of the bending three-body forces acting on the angular O_1–Sn–O_2 bond (see table 1). This is also consistent with the fact that the B_0/G_0 ratio for the SM is closer to the critical value than the corresponding AI result. Thus, the SM predicts a slightly less ductile material than the AI result.

The Debye temperatures obtained by both methods in this work are smaller than the corresponding experimental data, although differences are of ≈4%. This is also related to a small underestimation of the calculated mean sound velocities, as is observed in table 4.

Zone-center phonons, dispersion curves and the density of states. We have determined the zone-center phonon frequencies in the rutile phase in the pressure range 0–18 GPa by both AI and SM approaches. The Raman-active phonons do not involve Sn displacements since they occupy centrosymmetric positions in the lattice [37], while the infrared-active modes involve opposite motions of the Sn and O sublattices. We show in table 5 the AI and SM results for the zone-center optical phonon frequencies at $P = 0$ GPa, and compare them to other theoretical and experimental data. A general good agreement is observed between AI and experimental values, while major differences appear in the comparison with SM results, although the overall agreement is also good. The best agreements with experiment (<10%), and also between our AI and SM results, are found for the B_{2g} and B_{1g} Raman modes, and the A_{2u} and lowest E^3_u infrared modes. Additionally, good agreement is seen between our AI, SM and previous AI results for the higher B^1_{1u} mode, which unfortunately has not been measured.

On the other hand, our SM results for the remaining infrared E_u modes and the Raman A_{1g} and E_g modes exhibit discrepancies of 14%–25% with the experiments. The largest SM discrepancy corresponds to the A_{2g} silent mode, which is overestimated by ≈60% as compared to our AI and other theoretical results. The overall SM phonon performance is satisfactory considering that the model was adjusted mainly to the experimental rutile and $CaCl_2$ structures.

The dispersion relations were calculated along several symmetry directions in the Brillouin zone by means of the SM developed. The results are displayed in figure 3. This approach leads to stable phonon frequencies throughout the Brillouin zone. A qualitative good overall agreement between our SM results and the AI results of Parlinsky and Kawazoe [9] is attained for the low-frequency region. The slopes of the acoustic branches along different Brillouin-zone directions obtained by the two methods are in good accordance. These slopes are related to the SM results for the average sound velocities and the Debye temperatures shown in table 4, which are found to be in good agreement with the experimental values. However, an intermediate-frequency gap present in

Table 5. Zone-center optical phonons in rutile SnO_2 obtained at $P = 0$ by AI and SM calculations, compared with other theoretical and experimental assessments. All units are cm^{-1}.

Mode	AI[a]	SM[a]	LDA[b]	GGA[b]	Calc.[c]	Calc.[d]	Exp.[d]	Exp.[e]	Exp.[f]
B_{2g}	785	765	734	688	762	752	782	781	777
A_{1g}	677	728	617	577	638	646	638	637	636
E_g	500	402	462	432	470	441	476	476	475
B_{1g}	110	104	82	90	105	100	—	121	119
A_{2g}	372	589	320	314	366	398	—	—	—
B^1_{1u}	501	508	553	520	585	505	—	—	—
B^2_{1u}	160	202	138	134	147	140	—	—	—
A_{2u} (TO)	510	495	457	424	461	512	477	—	—
E^1_u (TO)	646	558	584	538	615	651	618	—	—
E^2_u (TO)	301	410	270	253	286	297	293	—	—
E^3_u (TO)	226	253	200	196	242	236	244	—	—

[a] Present work.
[b] Reference [43].
[c] Reference [9].
[d] Reference [16].
[e] Reference [5].
[f] Reference [6].

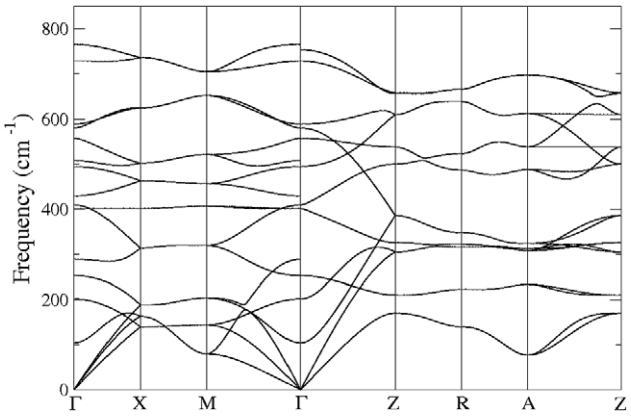

Figure 3. SM dispersion curves along symmetry directions of the Brillouin zone in SnO_2.

the AI results of [9] between 400 and 460 cm^{-1} is not reproduced by the SM. Also the SM dispersion in the high-frequency range shows major discrepancies with these AI results. Nevertheless, according to our experience in the study of nanostructure properties by means of bulk-developed SMs, such discrepancies in the high-frequency phonons do not appear to be a major problem for their applications at the nanoscale, as long as the overall agreement achieved with the model is qualitatively satisfactory. For example, a nice SM simulation of $KNbO_3/KTaO_3$ superlattices [44] was obtained even though the high-frequency phonons of $KNbO_3$ [45] were in only qualitatively good agreement with AI results [46]. The same occurred in SM simulations of nanostructured $BaTiO_3$ [47] and $PbTiO_3$ [48].

We have calculated the partial phonon density of states (PDOS) projected over different atoms with the present SM. We plot in figure 4 the PDOS for the Sn and O atoms. The Sn PDOS is also compared to available experimental data obtained from inelastic nuclear resonant scattering [49]. The calculated Sn band shows up in the low-frequency region from 0 to ≈400 cm^{-1} with four main peaks in fair qualitative agreement with experiments. Actually, the positions of the two highest peaks in the calculated Sn spectrum agree well with the experiment but there is no agreement in their relative intensities. The same is found for the lowest two peaks and also a shift of ≈40 cm^{-1} towards higher frequencies. Nevertheless, the agreement is satisfactory considering that the model was adjusted to reproduce mainly the rutile structure and not the phonon data. On the other hand, the O band is visualized mostly in the high-frequency region up to frequencies of ≈800 cm^{-1}. There is a mixture of the Sn and O peaks at ≈300 cm^{-1} and a smaller mixture of Sn and O characters in the broad band centered at ≈200 cm^{-1}. The large dispersion of the optical branches, which could be ascribed to the strong O–O interaction, may explain these mixtures and the absence of a gap (see also figure 3).

The behavior with pressure of the different phonon modes is another important issue studied in this work. The pressure dependences of the B_{2g}, A_{1g} and E_g Raman modes in the rutile phase were calculated up to pressures of ≈12 GPa. At pressures above the rutile–$CaCl_2$ transition pressure the rutile structure was retained as metastable. We compare in figure 5 the SM and AI results with corresponding experimental frequencies [6] for these Raman modes. We see that all frequencies increase linearly with increasing pressure in accordance with experiment. Moreover, the slopes of the phonons for the AI calculation are in excellent agreement with experiment for all modes. The SM results show also an excellent E_g mode slope agreement. The slopes of the remaining modes are less pronounced in the SM results than in those from experiment (see figure 5).

We have also studied the behavior with pressure of another Raman mode of B_{1g} symmetry. We plot in figure 6 the squared frequency of this mode as a function of pressure. Both AI and SM calculations show a soft behavior in the low-pressure rutile phase in accordance with the experiments.

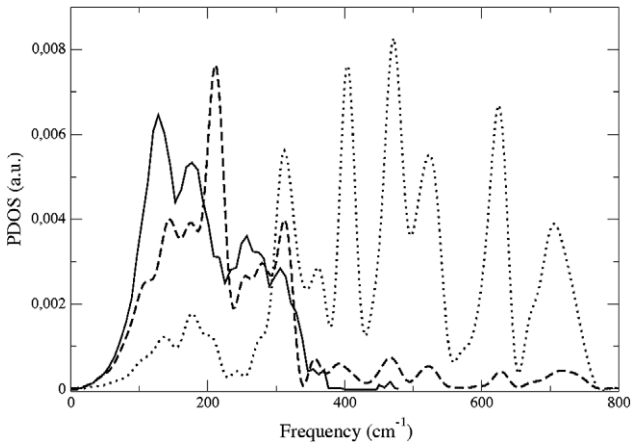

Figure 4. Partial phonon density of states (PDOS) calculated by means of the shell model developed in this work. We show the results for Sn (dashed lines) and O (dotted lines). Also shown is the experimental PDOS for Sn from [49] (solid lines). The spectra are normalized such that the area under the Sn curve is equal to 1.

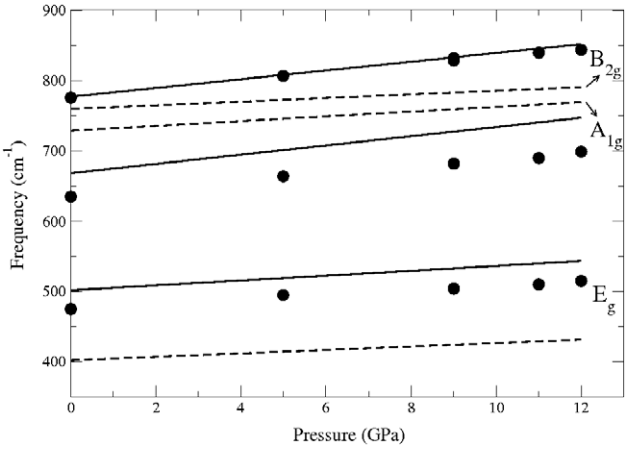

Figure 5. Frequencies of the B_{2g}, A_{1g} and E_g Raman modes as a function of pressure for the rutile phase of SnO_2. The AI and SM calculations are shown by solid and dashed lines respectively. The solid circles represent the experimental data from [6].

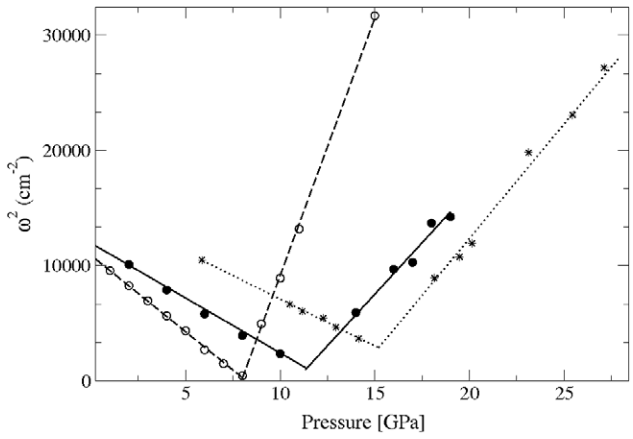

Figure 6. Pressure dependence of the squared frequency of the Raman soft mode of B_{1g}/A_g symmetry as a function of pressure. The AI and SM calculations are shown by solid and empty circles respectively. Linear fits to the AI and SM results are shown by solid and dashed lines respectively. The star symbols represent the experimental results from [6] while the dotted lines are linear fits to this data. The change in slope for each curve indicates the critical pressure for the rutile–$CaCl_2$ phase transition in each case (see explanations in the text).

Table 6. AI and SM results of the Grüneisen parameters γ for the Raman modes in the rutile phase of SnO_2 compared with other theoretical and experimental values.

Mode	AI[a]	SM[a]	Calc.[b]	Exp.[c]	Exp.[d]
B_{2g}	1.70	0.71	1.49	2.58	1.56
A_{1g}	2.08	1.00	1.33	3.64	1.73
E_g	1.46	1.23	1.29	3.20	1.52
B_{1g}	−10.67	−12.86	−14.17	−10.44	−8.56

[a] Present work.
[b] Reference [9].
[c] Reference [5].
[d] Reference [6].

This soft mode is precisely related to the rotation of the oxygen octahedra and couples to the shear elastic mode leading to the rutile–$CaCl_2$ phase transition [6]. The softening of the rutile B_{1g} mode with pressure is followed by hardening of the $CaCl_2$ A_g mode above P_c. This issue will be discussed in the next section in connection to the rutile–$CaCl_2$ ferroelastic transition.

We have evaluated the Grüneisen parameters γ_i using the following expression: $\gamma_i = (\partial\omega_i/\partial P)_0 B/\omega_i$, where B is the Bulk modulus and ω_i is the frequency of phonon i. The B values used in the above formula are those listed in table 2. The derivatives $\partial\omega_i/\partial P$ at $P = 0$ for the Raman modes of B_{1g}, B_{2g}, A_{1g} and E_g symmetries were determined by a linear regression of the curves depicted in figure 5. For the soft mode B_{1g} the linear regression was restricted to the range 0–2 GPa because of the non-linear behavior of this mode near P_c.

The AI and SM results for the Grüneisen parameters are compared in table 6 with other theoretical and experimental data. As a general feature, all Raman mode values of γ_i are positive except those of the soft mode, which are negative and substantially larger. Our AI results are in good agreement with experimental data [6]. Other experimental results show the same tendencies but in generally larger values of γ_i [5].

The Grüneisen constant value for the E_g mode obtained from the SM calculations shows the same good agreement. However, the SM γ_i values for the B_{2g} and A_{1g} modes are smaller than the experimental ones [6]. As for the soft B_{1g} mode, the value of γ_i is more negative than the AI and experimental data. This facts are visualized in figures 5 and 6 through the comparison of the SM, AI and experimental pressure dependences of the mode frequencies, as previously commented.

3.2. The rutile–$CaCl_2$ phase transition

In order to study the rutile–$CaCl_2$ phase transition as a function of pressure, it is important to choose an appropriate quantity to determine P_c. The second-order character of the transition prevented us from determining

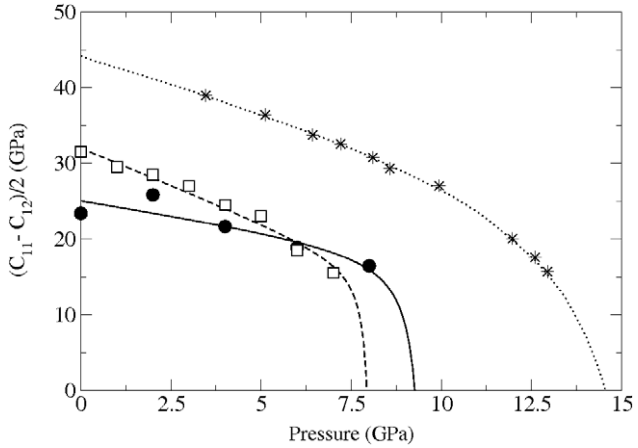

Figure 7. Pressure dependences of the elastic shear modulus C_{sm} obtained by fitting AI (solid circles and full line) and SM (empty squares and dashed line) results, compared with the analysis of experimental data (stars and dotted lines) [6].

the critical pressure by the usual common-tangent method, since the energy–volume curves of the two phases practically superpose. An alternative natural choice is the order parameter of the transition, i.e. the rotation angle of the oxygen octahedra around a z-axis through each Sn atom, since these rotations characterize the appearance of the $CaCl_2$-type structure upon overcoming P_c. However, as a consequence of its coupling to the lattice, this undergoes an orthorhombic distortion and, as a feedback effect, the oxygen octahedra distort. Thus, the rotation angle is not well defined in the high-pressure phase and therefore is not suitable for determining the transition pressure.

On the other hand, the B_{1g} mode of the rutile phase softens with increasing pressure and corresponds precisely to rotations of the oxygen octahedra. This mode becomes a mode of A_g symmetry in the high-pressure $CaCl_2$-type phase, and stabilizes with increasing pressure. The squared frequencies of these modes are linear functions of pressure and the intersection of the two lines clearly determines P_c [6]. By performing linear fits of the B_{1g} and A_g mode squared frequencies at different pressures we have determined the value of P_c from the intersection of these lines. The results of the AI and SM calculations are compared to the experimental findings in figure 6. From this plot, we have determined P_c as approximately 8 GPa and 11 GPa for the SM and AI calculations, respectively. These values are somewhat smaller than the experimental value of [6], ≈15 GPa (see figure 6). However, our AI result for P_c is in close agreement with the value of 11.8 GPa inferred from x-ray experiments [3]. Other first-principles calculations yield results of $P_c \approx 10.1$ [8] and 12 GPa [7], in agreement with the x-ray experiments and our AI calculations.

The underestimation of the SM critical pressure is related to the large absolute value obtained for the Grüneisen parameter in comparison to the corresponding value from our AI calculation. Actually, due to the linearity at low pressures of the soft mode squared frequency, it can be shown that smaller critical pressures correspond to larger negative values of γ (see figure 6 and table 6). This correlation is also verified in the first-principles calculations of [9].

The transition pressure can also be evaluated by studying the behavior of the elastic shear modulus $C_{sm} = (C_{11} - C_{12})/2$, which determines the softening of the TA mode of B_{1g} symmetry along 110 [33]. We employ the Landau theory of phase transitions to analyze the pressure behavior of C_{sm}. We follow the procedure of [6] to fit our data for C_{11} and C_{12} as functions of pressure. The results obtained from the AI and SM data are shown in figure 7 and compared with the same analysis of experimental data. The value of P_c obtained thus from the SM is 7.9 GPa, very close to the one obtained from the softening of the Raman B_{1g} mode. The analysis of the AI data leads to $P_c = 9.3$ GPa, somewhat lower than that from the Raman mode. The SM description of the pressure dependence of the elastic properties in relation to the structural transition is remarkable.

We have also studied the behavior with pressure of the lattice parameters. We show in figure 8 the AI and SM

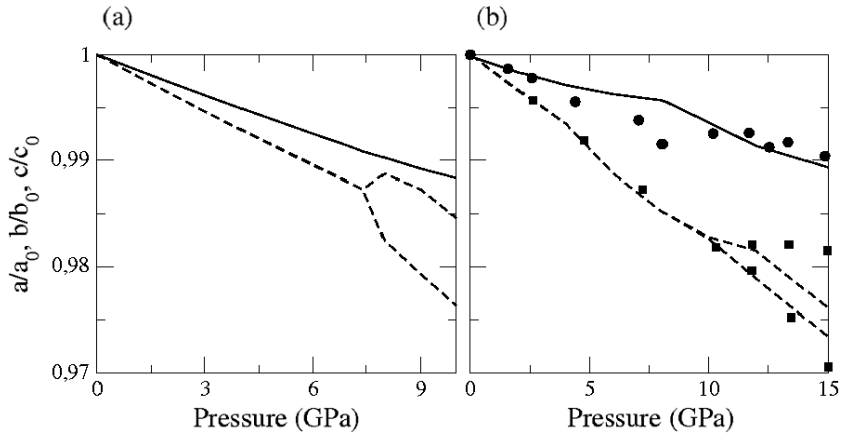

Figure 8. Normalized lattice parameters a/a_0, b/b_0 and c/c_0 of SnO_2 as a function of pressure. a_0, b_0 and c_0 are lattice constants at zero pressure. SM (a) and AI (b) results for lattice constants a and b are shown by dashed lines, while the corresponding results for c are shown by solid lines. Also shown in (b) are experimental results for a and b (solid squares) and c (solid circles) from [3].

results for the lattice parameters at different pressures and compare them to the experiment. The agreement between the AI results and experiments is very good. The accordance with the SM calculation is also qualitatively satisfactory. The curve of the lattice constant a in the rutile phase for the AI calculation was split into two curves at a pressure which is similar to the critical pressures obtained from figures 6 and 7. This is also verified in the SM case. This splitting corresponds to a differentiation of the basal lattice constants a and b in the orthorhombic $CaCl_2$-type structure. We find continuous changes in volume and lattice parameters at the transition from the $CaCl_2$ to the rutile structure, in agreement with previous x-ray diffraction studies [3] and confirming a second-order phase transition character. The slopes of the curves for the lattice parameter c are less pronounced than those of the curves for the basal parameters in both calculations, in accordance with experiments. This corresponds to a smaller degree of axial compressibility along the c direction in comparison to the corresponding value for the basal plane in the rutile phase, as is shown in table 2. The experimental degree of orthorhombicity (i.e. a–b) is qualitatively reproduced in both calculations.

4. Discussion and conclusion

With the aim of allowing future simulations of nanoscopic structures of SnO_2 and their behavior with pressure, we constructed an atomistic model of this compound in the framework of the shell model (SM) theory for ionic or partially covalent materials. In order to determine the parameters of such a model we performed *ab initio* (AI) calculations of the structural behavior of SnO_2 under pressure up to 20 GPa, which includes a structural transition from the ambient pressure rutile structure to a $CaCl_2$-type structure. We also studied AI the pressure behavior of the elastic constants, the phonon dispersion in the rutile phase and the softening of a zone-center B_{1g} phonon and the elastic shear modulus $(C_{11} - C_{12})/2$ on approaching the critical pressure P_c. Such a phonon involves a rotation of the Sn-centered O octahedra around the tetragonal axis of the rutile phase, which is the order parameter of the transition. A condensation of such a mode leads to the $CaCl_2$ phase. This mode couples to a transverse acoustic one of the same symmetry as described with the above mentioned elastic shear modulus. This also softens and leads to a pseudoproper ferroelastic transition from the tetragonal to an orthorhombic lattice. We also determined the bulk, shear and Poisson's moduli, the sound velocities and the Debye temperature. The AI results are in general good agreement with experimental measurements and previous AI calculations. The SM parameters have been adjusted primarily to reproduce the structural behavior with pressure and a good agreement was obtained with the AI and experimental data. Also the elastic properties are very satisfactorily reproduced. The SM calculated zone-center phonons in the rutile phase also show a satisfactory agreement with AI and experimental results. The SM phonon dispersion along symmetry directions of the Brillouin zone is in qualitatively good agreement with previous AI results [9]. Larger deviations appear in the high-frequency region; in particular a gap in the intermediate-frequency range is not present in the SM calculation. However, such discrepancies did not appear to be relevant for SM applications to nanostructures in previous perovskite simulations, as discussed above. On the other hand, assigning more weight to fit the high-frequency phonon dispersion reduces the accuracy of the description of the structure parameters and their distortions at the transition under pressure; we consider it important to take this into account to achieve a correct description of the material distortions at the nanoscale. As for P_c, the SM gives a value of 8 GPa, while AI and experimentally it was 10–11 and 11–15 GPa, respectively. The theoretical determinations of P_c were performed in three ways: (1) The crossing of the soft mode relations $\omega(B_{1g})$ versus P in the rutile phase with $\omega(A_g)$ versus P in the $CaCl_2$ phase. (2) The softening of the elastic shear modulus $(C_{11} - C_{12})/2$. (3) The appearance of an orthorhombic lattice distortion with increasing pressure. The AI results, in agreement with experiment, show an incomplete softening at P_c. Thus, the system jumps from one phase to the other before the first becomes actually unstable. This suggests that this phase transition is not completely displacive.

Acknowledgments

We acknowledge M Hu for the kind provision of experimental data which allowed the early development of the model for SnO_2. RAC would like to acknowledge support from the ANPCyT, Project PICT-CNPQ 066/08 and SECYT-UNNE. This work was partially supported through Grants PICT-2008 No. 1867 (ANPCyT) and PIP No. 2195 (CONICET). JL, SK, and RLM acknowledge additional support from CONICET.

References

[1] Batzill M and Diebold U 2005 *Prog. Surf. Sci.* **79** 47
[2] Pan J, Shen H and Mathur S 2012 *J. Nanotechnol.* **2012** 917320
[3] Haines J and Leger J M 1997 *Phys. Rev.* B **55** 11144
[4] Shieh S R, Kubo A, Duffy T S, Prakapenka V B and Shen G 2006 *Phys. Rev.* B **73** 014105
[5] Peercy P S and Morosin B 1973 *Phys. Rev.* B **7** 2779
[6] Hellwig H, Goncharov A F, Gregoryanz E, Mao H-K and Hemley R J 2003 *Phys. Rev.* B **67** 174110
[7] Gracia L, Beltrán A and Andrés J 2007 *J. Phys. Chem.* B **111** 6479
[8] El Haj Hassan F, Alaeddine A, Zoaeter M and Rachidi I 2005 *Int. J. Mod. Phys.* B **19** 4081
[9] Parlinski K and Kawasoe Y 2000 *Eur. Phys. J.* B **13** 679
[10] Cohen R E 1992 First-principles predictions of elasticity and phase transitions in high pressure SiO_2 and geophysical implications *High Pressure Research in Mineral Physics: Application to Earth and Planetary Science (Ise, Japan, Jan. 1991)* ed M H Manghnani and Y Syono, pp 425–32
[11] Tsuchida Y and Yagi T 1989 *Nature* **340** 217
[12] Kingma M J, Cohen R E, Hemley R J and Mao H K 1995 *Nature* **374** 243
[13] Karki B B, Warren M C, Stixrude L, Ackland G J and Crain J 1997 *Phys. Rev.* B **55** 3465
[14] Togo A, Oba F and Tanaka I 2008 *Phys. Rev.* B **78** 134106
[15] Zhang L, Wang Y, Cui T, Li Y, Li Y, He Z, Ma Y and Zou G 2007 *Phys. Rev.* B **75** 144109

[16] Katiyar R S, Dawson P, Hargreave M M and Wilkinson G R 1971 *J. Phys. C: Solid State Phys.* **4** 2421
[17] Gervais F and Kress W 1985 *Phys. Rev.* B **31** 4809
[18] Sato T and Asari T 1995 *J. Phys. Soc. Japan* **64** 1193
[19] Chang E and Graham E K 1975 *J. Geophys. Res.* **80** 2595
[20] Liu C M, Chen X R and Ji G F 2011 *Comput. Mater. Sci.* **50** 1571
[21] Koval S, Burriel R, Stachiotti M G, Castro M, Migoni R L, Moreno M S, Varela A and Rodriguez C O 1999 *Phys. Rev.* B **60** 14496
[22] Koval S, Stachiotti M G, Migoni R L, Moreno M S, Mercader R C and Peltzer y Blancá E L 1996 *Phys. Rev.* B **54** 7151
[23] Sepliarsky M and Cohen R E 2011 *J. Phys.: Condens. Matter* **23** 435902
[24] Lasave J, Dominguez F, Koval S, Stachiotti M G and Migoni R L 2005 *J. Phys.: Condens. Matter* **17** 7133
[25] Lasave J, Kohanoff J, Migoni R L and Koval S 2009 *Physica* B **404** 2736
[26] Soler J M, Artacho E, Gale J D, Garcia A, Junquera J, Ordejon P and Sanchez-Portal D 2002 *J. Phys.: Condens. Matter* **14** 2745
[27] Troullier N and Martins J L 1991 *Phys. Rev.* B **43** 1993
[28] Kleinman L and Bylander D M 1982 *Phys. Rev. Lett.* **48** 1425
[29] Caravaca M A and Casali R A 2005 *J. Phys.: Condens. Matter* **17** 5795
[30] Caravaca M A, Miño J C, Perez C, Casali R A and Ponce C A 2009 *J. Phys.: Condens. Matter* **21** 015501
[31] Musgrave M J P 1970 *Crystal Acoustics: Introduction to the Study of Elastic Waves and Vibrations in Crystals* (San Francisco, CA: Holden-Day)
[32] Ravindran P, Fast L, Korzhavyi P A, Johnnsson B, Wills J and Eriksson O 1998 *J. Appl. Phys.* **84** 4891
[33] Nye J F 1957 *Physical Properties of Crystals* (Oxford: Oxford University Press)
[34] Katiyar R S 1970 *J. Phys. C: Solid State Phys.* **3** 1087
[35] Gale J 1997 *J. Chem. Soc. Faraday Trans.* **93** 629
[36] Zhu B, Liu C, Lv M, Chen X, Zhu J and Ji G 2011 *Physica* B **406** 3508
[37] Peltzer y Blancá E L, Svane A, Christensen N E, Rodriguez C O, Cappannini O M and Moreno M S 1993 *Phys. Rev.* B **48** 15712
[38] Voigt W 1928 *Lehrbuch der KrystallPhysik* (Leipzig: Teubner)
[39] Reuss A 1929 *Z. Angew. Math. Mech.* **9** 49
[40] Hill R 1952 *Proc. Phys. Soc.* A **65** 349
[41] Pugh S F 1954 *Phil. Mag.* **45** 823
[42] Lieberman R C 1973 *Phys. Earth Planet. Inter.* **7** 461
[43] Borges P D, Scolfaro L M R, Leite Alves H W and da Silva E F Jr 2010 *Theor. Chem. Acc.* **126** 39
[44] Sepliarsky M, Phillpot S R, Wolf D, Stachiotti M G and Migoni R L 2001 *J. Appl. Phys.* **90** 4509
[45] Sepliarsky M, Stachiotti M G, Migoni R L and Rodriguez C O 1999 *Ferroelectrics* **234** 9
[46] Yu R and Krakauer H 1995 *Phys. Rev. Lett.* **74** 4067
[47] Tinte S and Stachiotti M G 2001 *Phys. Rev.* B **64** 235403
Stachiotti M G 2004 *Appl. Phys. Lett.* **84** 251
[48] Sepliarsky M, Stachiotti M G and Migoni R L 2006 *Phys. Rev. Lett.* **96** 137603
Stachiotti M G and Sepliarsky M 2011 *Phys. Rev. Lett.* **106** 137601
[49] Hu M Y 1999 *PhD Thesis* Northwestern University, Evanston, IL